CFD Analysis of Near-Field Exhaust Thermodynamics in Hydrogen-Fuelled Jet Engines and Their Implications for Contrail Formation

A. Daruka*
Oslo International School, Gamle Ringeriksvei 53, 1318 Bekkestua, Oslo, Norway

Krish A.†
The Doon School, Dehradun, Uttarakhand, 248001, India

Ankit Bansal‡
Indian Institute of Technology, Roorkee, Haridwar Highway, Uttarakhand 247667, India

Hydrogen combustion is increasingly recognised as a key pathway toward decarbonising aviation. However, while it eliminates carbon dioxide emissions, it also produces substantially more water vapour and virtually no soot, creating competing effects for contrail formation. The near-field thermodynamics of such exhausts remain poorly characterised, even though they critically determine whether supersaturation, and thus contrail formation, occurs immediately downstream of the engine. Therefore, this study aims to performs a computational analysis of near-field exhaust flows in hydrogen-fuelled jet engines using the rhoSimpleFoam solver in OpenFOAM. A steady, compressible Reynolds-Averaged Navier–Stokes (RANS) framework with a k–ω SST turbulence model is applied to simplified nozzle geometries for kerosene and hydrogen cases. The simulations resolve the coupled pressure, velocity, and temperature fields, from which the local saturation ratio S is computed to identify supersaturated regions conducive to contrail formation. Our simulation results show a clear relation between near-field plume behaviour and humidity fraction and ambient pressure. Specifically, the maximum saturation ratio increases almost linearly with water vapour fraction, while lower ambient pressures cause longer but less supersaturated plumes. Overall, kerosene exhausts remain sub-saturated, whereas hydrogen cases consistently exceed saturation, confirming a stronger thermodynamic tendency toward contrail initiation.

I. Nomenclature

U	=	Velocity vector field ($\mathrm{m\,s^{-1}}$)
U_{in}	=	Inlet velocity magnitude ($\mathrm{m\,s^{-1}}$)
p_{amb}	=	Ambient pressure (Pa)
$p_{\mathrm{H_2O}}$	=	Partial pressure of water vapour (Pa)
$p_{\mathrm{sat}}(T)$	=	Saturation vapour pressure at temperature T (Pa)
S	=	Saturation ratio = $p_{\mathrm{H_2O}}/p_{\mathrm{sat}}(T)$ (–)
h	=	Specific enthalpy ($\mathrm{J\,kg^{-1}}$)
T	=	Static temperature field (K)
T_{in}	=	Inlet temperature (K)
ρ	=	Density ($\mathrm{kg\,m^{-3}}$)
μ	=	Dynamic viscosity (Pa s)
ν	=	Kinematic viscosity ($\mathrm{m^2\,s^{-1}}$)
$y_{\mathrm{H_2O}}$	=	Water vapour mass fraction (–)

*Student, Department of Physics and AIAA Student Member: 1856657, High School Category.
†Student, Department of Physics and AIAA Student Member: 1862371, High School Category.
‡Professor, Department of Mechanical and Industrial Engineering, Faculty Advisor.

ω = Specific dissipation rate (s^{-1})
Φ = Viscous dissipation term ($W\,m^{-3}$)
T_{crit} = Critical temperature for contrail formation (K)
τ = Viscous stress tensor

II. Introduction and Background

The aviation sector is a growing contributor to climate forcing, responsible not only for long-lived carbon dioxide (CO_2) emissions but also for short-lived non-CO_2 effects such as contrails and the release of nitrogen oxides [1, 2]. Together, these short-lived forcers are estimated to contribute more than half of aviation's total radiative forcing, making them central to any strategy for climate-neutral flight. As conventional kerosene combustion faces increasing scrutiny, hydrogen has emerged as a promising alternative fuel due to its carbon-free exhaust and high energy density [3].

However, hydrogen combustion introduces two competing thermodynamic effects that make its climatic implications not straightforward [4]. On one hand, the complete oxidation of hydrogen produces approximately 2.6 times more water vapour per unit of energy than kerosene, which enhances the likelihood of contrail formation. On the other hand, hydrogen flames generate negligible soot, drastically reducing the availability of ice-nucleating particles necessary for persistent contrail growth. While the microphysics of contrail formation has been discussed in prior studies [4], the thermodynamic conditions that govern when and where supersaturation first occurs within the engine exhaust remain under-explored. Understanding these underlying flow and temperature fields is therefore essential to interpreting the broader climate impact of hydrogen-fuelled propulsion.

While several studies have analysed contrail evolution under idealised or far-field conditions [4–6], the near-field thermodynamics of the exhaust remains insufficiently investigated. Current prediction frameworks neglect the confined expansion, shear, and turbulent mixing that define the initial plume. This is important as near-field processes determine whether the mixture locally cools below saturation and thus whether condensation can even begin. Variations in fuel composition, ambient pressure, and outlet temperature all can significantly alter local temperature, density, and humidity distributions [7–9], fundamentally influencing the thermodynamic pathway to supersaturation and ice-crystal nucleation [10].

Some efforts have begun to address this gap. Khou et al. (2015) [11] performed a three-dimensional RANS-based simulations of contrail formation using realistic aircraft geometry. They showed that supersaturation and ice growth are strongly governed by near-field humidity and jet–vortex interactions. Cantin et al. (2025) [12] extended this approach with a coupled CFD–microphysics solver to study the role of sulfur content, soot concentration, and organics in contrail development, highlighting sensitivity to exhaust composition. Tegethoff and Wheeler (2025) [13] developed a framework to resolve condensation and freezing kinetics in the near-field exhaust. They showed that nozzle geometry and vapour content critically determine early-phase thermodynamics. Lottermoser and Unterstrasser (2025) [14] introduced the RadMod framework, where they captured self-similar plume expansion in a reduced-order system. Other studies, such as by Bier et al. (2025) [15] incorporated hydrogen combustion conditions into contrail parametrisations, confirming that exhaust composition and bypass/core flow structure strongly influence the saturation ratio at the engine exit.

Together, these works emphasise that near-field modelling rather than far-field approximations is essential for understanding contrail formation under hydrogen combustion.

In the present study, we address this research gap through steady, compressible CFD simulations of a simplified hydrogen jet exhaust using the rhoSimpleFoam solver in OpenFOAM [16]. Instead of resolving detailed combustion chemistry, the model isolates the influence of thermodynamic expansion on the exhaust's pressure, velocity, and temperature fields—quantities that dictate post-exit cooling and potential supersaturation. A Reynolds-Averaged Navier–Stokes (RANS) framework with a k–ω shear-stress transport (SST) turbulence model is employed to compute steady-state solutions for multiple inlet conditions representing kerosene- and hydrogen-fuelled cases. From these, the outlet thermodynamic properties are post-processed to compute the local saturation ratio,

$$S = \frac{p_{H_2O}}{p_{sat}(T)},$$

which quantifies whether the exhaust mixture achieves supersaturation conditions necessary for condensation.

This work thereby establishes a framework linking in-nozzle flow physics with contrail formation potential. By systematically quantifying how variations in temperature, hydrogen fraction, and pressure affect supersaturation onset, the study provides a foundation for more realistic assessments of hydrogen propulsion technologies and their climatic implications.

III. Methodology and OpenFOAM Setup

This section provides an overview of the key features of our simulation setup and what parameters we varied between individual cases.

A. Geometry and Mesh

The computational domain that we used consists of a simplified cylindrical nozzle section connected to a rectangular exhaust region, as shown in Figure 1. The cylindrical portion represents the engine nozzle exit, while the rectangular box models the near-field region where the exhaust expands and mixes with the surrounding flow. This simplified geometry captures the essential thermodynamic evolution of the jet plume while avoiding the complexities of a full combustor assembly due to computational constraints.

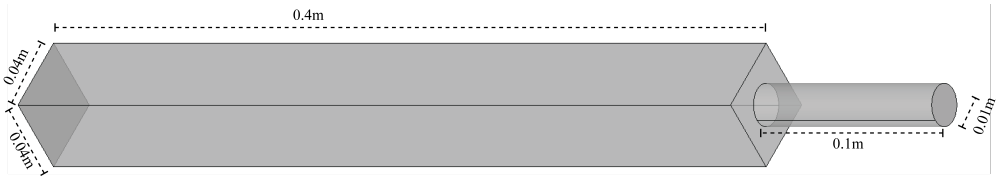

Fig. 1 The computational domain that we used for analysis. The nozzle is defined as a cylinder with diameter 0.01m and height of 0.1m. The expansion region is defined as a cuboid with length 0.4m, along with width and height of 0.04m.

The inlet is defined at the circular face of the nozzle, where we set temperature and velocity boundary conditions. The outlet is at the downstream face of the rectangular domain, this ensures that our flow variables become nearly uniform. All other faces are treated as slip walls to simulate an open flow environment.

Our final mesh shown in Figure 2 is hexahedral and uniform. We added further refinement in the form of a sub-mesh near the nozzle exit to resolve gradients in temperature, pressure, and velocity during jet expansion.

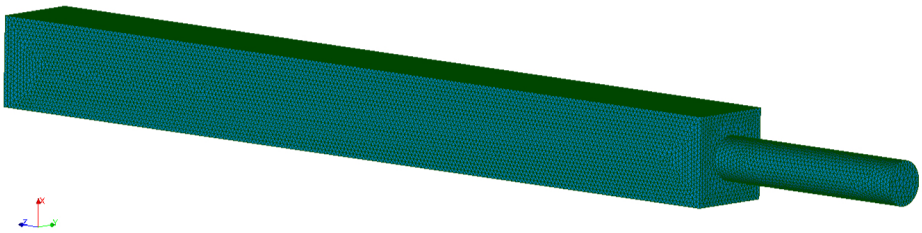

Fig. 2 The computational mesh of the nozzle and exhaust. The mesh is fully hexahedral, and we locally refined near the nozzle exit to capture the steep gradients during expansion.

The mesh was created inside the SALOME environment [17] and exported as a .unv file to be used inside OpenFOAM.

B. Governing Equations and modelling

The flow was modelled as a steady, compressible, turbulent gas governed by the Reynolds-Averaged Navier–Stokes (RANS) equations implemented in the *rhoSimpleFoam* solver. We define air using the ideal gas law and the specific enthalpy–temperature relation through the hePsiThermo model.

The governing equations are as follows:

First, the continuity equation,

$$\nabla \cdot (\rho \mathbf{U}) = 0. \tag{1}$$

Then, the momentum equation that represents the balance of pressure, viscous, and body forces,

$$\nabla \cdot (\rho \mathbf{U}\mathbf{U}) = -\nabla p + \nabla \cdot \boldsymbol{\tau} + \rho \mathbf{g}. \tag{2}$$

The viscous stress tensor, which accounts for both molecular and turbulent momentum diffusion,

$$\nabla \cdot (\rho \mathbf{U} h) = \nabla \cdot (\alpha_{\text{eff}} \nabla h) + \frac{Dp}{Dt} + \Phi, \tag{3}$$

where ρ is the density, $\mathbf{U}$ is the velocity vector, p is the static pressure, and h is the specific sensible enthalpy. The viscous stress tensor $\boldsymbol{\tau}$ is defined as

$$\boldsymbol{\tau} = \mu_{\text{eff}} \left[\nabla\mathbf{U} + (\nabla\mathbf{U})^T\right] - \frac{2}{3}\mu_{\text{eff}}(\nabla \cdot \mathbf{U})\mathbf{I}, \tag{4}$$

where $\mu_{\text{eff}} = \mu + \mu_t$ is the effective viscosity, comprising the molecular viscosity μ and the turbulent (eddy) viscosity μ_t. The effective thermal diffusivity is given by $\alpha_{\text{eff}} = \mu_{\text{eff}}/(\rho c_p \,\text{Pr}_{\text{eff}})$, and Φ represents viscous dissipation.

The ideal gas law,

$$p = \rho R T, \tag{5}$$

where R is the specific gas constant and T is the static temperature. For hePsiThermo, the sensible enthalpy is related to temperature through $h = c_p T$.

Turbulence effects were modelled using the k–ω shear-stress transport (SST) model, which provides robust predictions in both near-wall and free-shear regions. The two transport equations are

$$\nabla \cdot (\rho\mathbf{U}k) = \nabla \cdot [(\mu + \sigma_k\mu_t)\nabla k] + P_k - \beta^*\rho k\omega \tag{6}$$

$$\nabla \cdot (\rho\mathbf{U}\omega) = \nabla \cdot [(\mu + \sigma_\omega\mu_t)\nabla\omega] + \alpha\frac{\omega}{k}P_k - \beta\rho\omega^2, \tag{7}$$

where k is the turbulent kinetic energy, ω is the specific dissipation rate, and P_k represents the turbulence production term.

The equations are solved in a segregated manner using the SIMPLE algorithm, which iteratively couples the pressure and velocity fields.

$$\text{Momentum equation: } \mathbf{U}^* = \mathbf{U}^n + A^{-1}(b - \nabla p^n), \tag{8}$$

$$\text{Pressure correction: } \nabla \cdot (\rho A^{-1}\nabla p') = \nabla \cdot (\rho\mathbf{U}^*), \tag{9}$$

$$\text{Velocity correction: } \mathbf{U}^{n+1} = \mathbf{U}^* - A^{-1}\nabla p', \tag{10}$$

where A denotes the discretised momentum matrix, b is the source term, and p' is the pressure correction. This iterative process continued for 200 iterations across all cases as this was when the residuals dipped below the convergence criteria.

C. Thermophysical model

Our thermophysical model *hePsiThermo* model computes thermodynamic variables from pressure ($\psi = 1/RT$) and temperature while maintaining consistency between density, enthalpy, and pressure. We chose this model as hePsiThermo explicitly couples enthalpy with the ideal-gas law. This ensures an accurate representation of density and temperature variations that arise from nozzle expansion and exhaust cooling.

In our setup, air was treated as a single perfect-gas species with a molecular weight of $28.9\,\text{g mol}^{-1}$, constant specific heat $C_p = 1005\,\text{J kg}^{-1}\,\text{K}^{-1}$, dynamic viscosity $\mu = 1.82 \times 10^{-5}\,\text{Pa s}$, and Prandtl number $Pr = 0.71$. These values are typical high-temperature air properties and ensure numerical stability across all three inlet cases.

D. Boundary and Initial Conditions

1. Temperature, Velocity, and Specific Enthalpy

For our study, 12 distinct inlet configurations were defined to represent varying exhaust compositions, ambient pressure values, and flow regimes relative to kerosene and hydrogen combustion.

The first 3 combustions correspond to Kerosene-like exhaust. Configurations 1 and 2 operate at similar conditions, with an exception of a change in p_{amb}. Configuration 3 maintains similar conditions with the exceptions of the inlet temperature T_{in} being 1500 K. These configurations serve as our reference exhaust, and provide a baseline qualitative understanding of how changes in inlet temperatures (T_{in}) and ambient pressure (p_{amb}) affect plume formation.

Configurations 4 to 7 correspond to Hydrogen cases operating at at differing values of p_{H_2O} (Pa), allowing us to isolate the p_{H_2O} driven influences on near-field plume formation. In these configurations, T_{in}, is fixed at 1250 (K).

Configurations 8 to 10 correspond to hydrogen exhaust cases operating at fixed inlet temperatures but operating with 3 distinct p_{amb} values that aim to simulate standard atmospheric, mid-altitude, cruise-level, and high altitude pressure values.

Table 2 Boundary conditions for the Kerosene cases.

ID	Fuel	U_{in} (m s^{-1})	T_{in} (K)	h (kJ kg^{-1})	p_{amb} (Pa)	p_{H_2O} (Pa)
1	Kerosene	100	1250	1005	23800	2856.0
2	Kerosene	100	1250	1005	101,325	12200.0
3	Kerosene	100	1500	1507.5	101,325	12200.0

Table 3 Boundary conditions for the Hydrogen fuel-cell cases where we varied p_{H_2O}

ID	Fuel	U_{in} (m s^{-1})	T_{in} (K)	h (kJ kg^{-1})	p_{amb} (Pa)	p_{H_2O} (Pa)
4	Hydrogen	100	1250	1005	101,325	22291.5
5	Hydrogen	100	1250	1005	101,325	30397.5
6	Hydrogen	100	1250	1005	101,325	38503.5
7	Hydrogen	100	1250	1005	101,325	46609.5

Table 4 Boundary conditions for the Hydrogen fuel-cell cases where we varied p_{amb} and kept yH_2O constant.

ID	Fuel	U_{in} (m s^{-1})	T_{in} (K)	h (kJ kg^{-1})	p_{amb} (Pa)	p_{H_2O} (Pa)
8	Hydrogen	100	1250	1005	101,325	33437.3
9	Hydrogen	100	1250	1005	50,000	16500.0
10	Hydrogen	100	1250	1005	23800	7854.0

Across all cases, the inlet velocity magnitude was capped at 100 m s^{-1} to ensure numerical stability and maintain Courant number targets on the chosen mesh. Higher, physically representative exhaust velocities can be accommodated in transient LES or hybrid simulations, but these require finer temporal resolution and mesh refinement to avoid non-physical values and convergence difficulties.

IV. Results

A. Post-Processing Methodology

After selecting the 10 configurations, we ran the solver in OpenFOAM and post-processed in Paraview [18]. During post-processing we recorded two key variables: the Axial Length of the plume formed and the maximum saturation ratio S_{max}.

These variables were computed using the following formulas.

Firstly, the water vapour partial pressure was estimated assuming an ideal gas mixture through Dalton's law [19]:

$$p_{H_2O} = y_{H_2O}\, p, \tag{11}$$

where y_{H_2O} is the mole fraction and p is the local static pressure. In the absence of a solved species transport field, the humidity fraction was approximated as $y_{H_2O} = 0.12$ for the kerosene baseline and, where held constant, $y_{H_2O} = 0.33$ for the hydrogen-fuelled cases.

Next, the saturation vapour pressure $p_{sat}(T)$ was calculated using the empirical Tetens formula [20]:

$$p_{sat}(T) = 610.78 \exp\left[\frac{17.27(T - 273.15)}{T - 35.85}\right], \tag{12}$$

where T is expressed in Kelvin. This yields p_{sat} in pascals. The ratio S was subsequently visualised in ParaView, and regions with $S > 1$ were identified as thermodynamically favourable for condensation and potential contrail formation.

B. Plume Plots

For the plots, we set a threshold to show areas of the exhaust where $S < 1$. This was our unsaturated region.

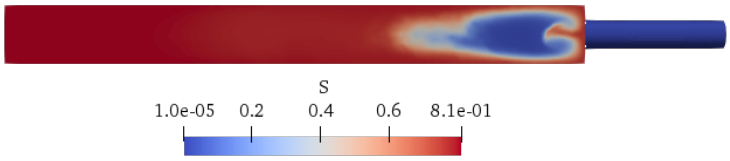

(a) Kerosene - Case 1

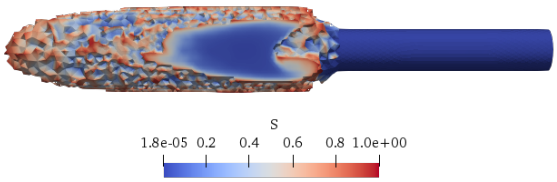

(b) Kerosene - Case 2

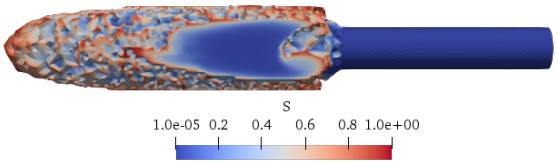

(c) Kerosene - Case 3

Fig. 3 Plume views for kerosene exhaust at $U_{in} = 100\ \text{m s}^{-1}$ with $T_{in} = 1250$–1500 K and $p_{\text{amb}} = 23{,}800$–$101{,}325$ Pa.

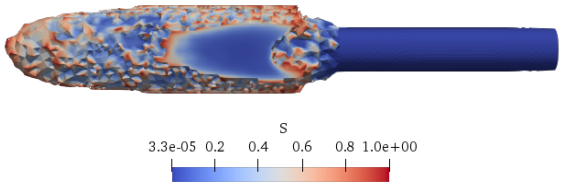

(a) Hydrogen - Case 4

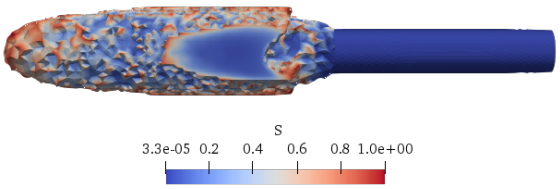

(b) Hydrogen - Case 5

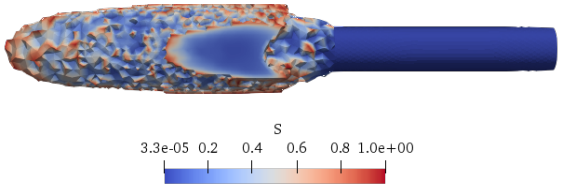

(c) Hydrogen - Case 6

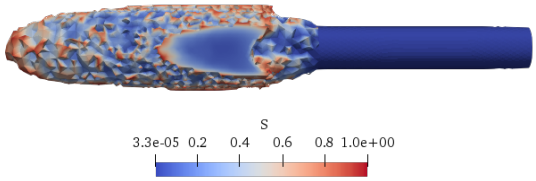

(d) Hydrogen - Case 7

Fig. 4 Plume views for hydrogen exhaust at $U_{in} = 100\ \text{m s}^{-1}$, $T_{in} = 1250$ K, and varying $p_{\text{amb}} = 22{,}291$–$46{,}609$ Pa.

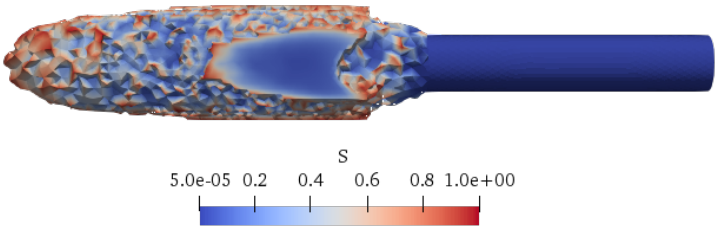

(a) Hydrogen - Case 8

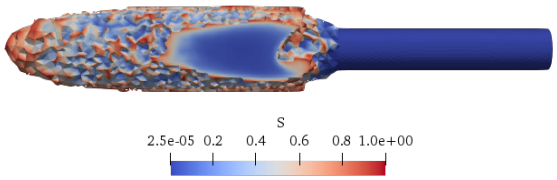

(b) Hydrogen - Case 9

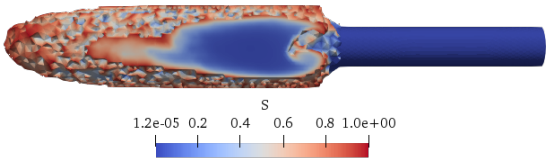

(c) Hydrogen - Case 10

Fig. 5 Plume views for hydrogen exhaust at $U_{in} = 100\ \mathrm{m\,s^{-1}}$, $T_{in} = 1250$ K, and varying $p_{\mathrm{H_2O}} = 7{,}854$–$33{,}437$ Pa.

C. Parameter Distributions

We organised our raw data into a tabular form to provide an overview of the inlet conditions and corresponding plume characteristics obtained from the simulations.

Here, the maximum supersaturation ratio $S_{\max}$ and the axial length of the plume core are extracted from the post-processed plume views shown earlier. We then proceeded to plot the key output parameters against the inlet and

Table 5 Summary of inlet conditions and corresponding plume characteristics recorded.

Case ID	T_{in} (K)	y_{H2O}	P_{amb} (Pa)	Axial length (m)	$S_{\max}$
1	1250	0.12	23800	–	0.81
2	1250	0.12	101325	0.159	3.44
3	1500	0.12	101325	0.164	3.44
4	1250	0.22	101325	0.253	6.31
5	1250	0.30	101325	0.250	8.61
6	1250	0.38	101325	0.248	10.91
7	1250	0.46	101325	0.248	13.20
8	1250	0.33	101325	0.250	9.47
9	1250	0.33	50000	0.257	4.67
10	1250	0.33	23800	0.267	2.22

ambient conditions in order to quantify the observed plume trends.

These correlations help identify how the ambient pressure and water-vapour fraction influence both the axial plume length and $S_{\max}$.

However, because we calculated $S_{\max}$ using $p_{\mathrm{H_2O}} = y_{\mathrm{H_2O}}\, p$, our approach does not explicitly account for the progressive dilution of water vapour as the exhaust mixes with the surrounding air, and therefore the resulting supersaturation ratios represent the undiluted vapour concentration within the core of the plume. Although this simplification may overestimate $S_{\max}$ in regions of intense mixing, it provides a consistent basis for comparing relative trends across different fuel types and boundary conditions.

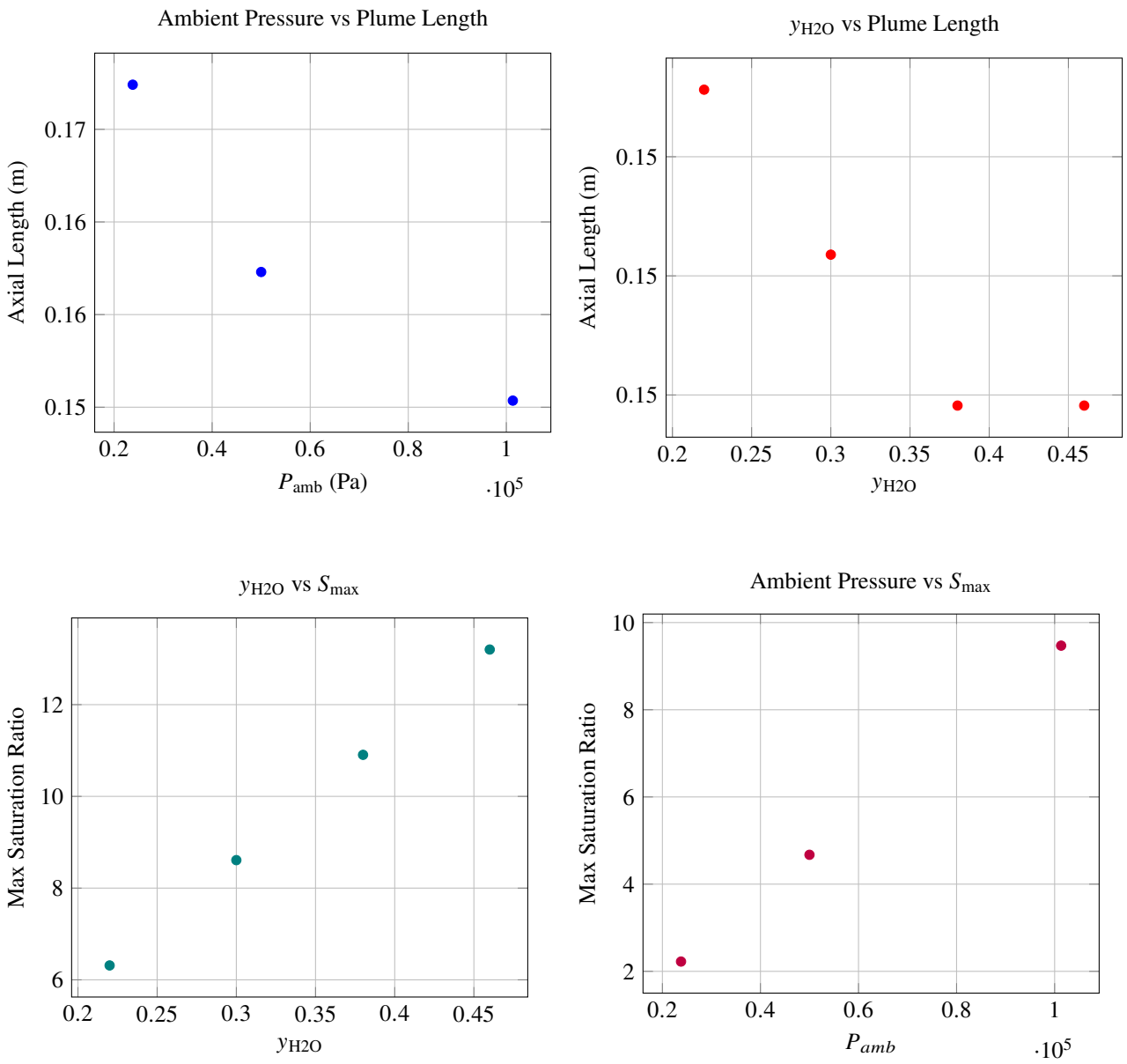

Fig. 6 Our graphs showing relationships between plume length, humidity fraction, ambient pressure, and maximum saturation ratio.

D. Dicussion of results

Our simulated cases exhibit a small number of clear, repeatable patterns across fuel type, ambient pressure, and water-vapour content:

- The kerosene cases produce substantially lower maximum saturation ratios than the hydrogen cases (shown in the legends of Figure 3). Kerosene runs show S_{max} values near or below 1 in the low-pressure case (e.g. $S_{max} \approx 0.81$ when $p_{amb} = 23800$ Pa) and modestly above 1 in other kerosene runs ($S_{max} \approx 3.44$), while hydrogen cases reach considerably larger peak values (range $S_{max} \approx 2.22$ to 13.20). This indicates a systematically greater tendency toward local supersaturation for the hydrogen exhausts under the tested conditions.
- Axial plume lengths are consistently longer in the hydrogen cases than in the kerosene cases. Kerosene axial lengths are near ~0.16 m, whereas hydrogen plumes in our parametrisation extend to ~0.25–0.27 m (Table 5). Hydrogen exhausts therefore maintain thermodynamic structure over a longer near-field distance in these simulations.
- For hydrogen cases at fixed ambient pressure, S_{max} increases with the exhaust water vapour mass fraction. For

example, as y_{H_2O} rises from 0.22 to 0.46 the reported S_{max} climbs from ~6.3 to ~13.2. This demonstrates that, within our model, water-vapour content is a primary control on peak saturation.

- Decreasing ambient pressure (moving from 101,325 Pa to 50,000 Pa and 23,800 Pa in the hydrogen subset) reduces the reported peak saturation ratios (e.g. $S_{max} \approx 9.47$ at 101,325 Pa down to ≈ 4.67 and ≈ 2.22 at lower pressures). At the same time, the axial length associated with the near-field plume increases slightly as ambient pressure falls (from ~0.25 m to ~0.27 m). In short, lower ambient pressure in these cases produces more extended but less intensely supersaturated near-field regions.
- Across the hydrogen cases there is a weak inverse tendency between axial length and S_{max}. The largest S_{max} values occur at slightly smaller axial lengths (closer to the exit), while cases with reduced peak saturation tend to show modestly longer axial extents. This suggests that stronger, localized cooling near the nozzle produces higher peak saturation but confines it to a shorter downstream distance.
- Figure 6 shows the variation of maximum saturation ratio (S_{max}) with ambient pressure (p_{amb}). The results indicate a clear positive correlation, where increasing p_{amb} leads to higher S_{max}. This behaviour arises because higher ambient pressures enhance gas density, thereby increasing the partial pressure of water vapour in the exhaust plume. As a result, the local thermodynamic conditions favour condensation more readily, elevating the peak supersaturation ratio. Conversely, at lower pressures, reduced molecular collisions and lower vapour partial pressures inhibit saturation, explaining the lower S_{max} observed. This trend aligns with the expected dependence of contrail formation potential on ambient static pressure in near-field exhaust regions.

V. Further discussion and conclusion

A. Comparison of the Three Flow Cases

Direct comparison across the kerosene and hydrogen configurations highlights two robust outcomes from our study. First, hydrogen exhausts show consistently larger axial plume extents and substantially higher peak saturation ratios than the kerosene cases: hydrogen S_{max} values exceed those of kerosene by factors of several (Table 5), and the hydrogen plumes persist farther downstream in the near-field (axial lengths $\approx$ 0.25–0.27m for the Hydrogen cases versus $\approx$ 0.16m for the kerosene cases). Second, the sensitivity analysis indicates that the maximum saturation ratio is strongly controlled by the water vapour mass fraction (y_{H_2O}) and ambient pressure. Increasing y_{H_2O} produces an approximately monotonic rise in S_{max}, while reducing ambient pressure tends to shorten the axial length over which supersaturation occurs but does not decrease peak S_{max}.

Interpretational caution is required because the three flow families (kerosene, baseline hydrogen, and hydrogen variants) differ in both composition and imposed ambient conditions. Nevertheless, for the simplified nozzle geometry and thermophysical assumptions used here, hydrogen exhausts are more prone to producing immediate post-exit supersaturation. Whether that supersaturation evolves into persistent, climate-relevant contrails will depend on microphysical availability (soot/ice nuclei), ambient temperature and humidity profiles beyond the near-field, and the transient nature of vortex–plume interactions that were not fully resolved in our steady-RANS study.

B. Limitations and Future Work

This study deliberately adopted a simplified, steady RANS approach and an ideal-gas single-mixture thermophysical model to isolate the hydrodynamic and thermodynamic controls on near-field saturation. That simplification imposes several limitations. Most notably, (i) steady RANS does not resolve transient vortex rings and intermittent shear-layer dynamics that can create localized, short-duration extrema in temperature and humidity; (ii) the model omits soot and other aerosol species that provide heterogeneous ice-nucleating sites; (iii) chemical non-equilibrium, multi-species transport, and detailed thermodynamic behaviour at low temperatures are not represented; and (iv) inlet velocities were capped for numerical stability, so the parameter space does not fully cover realistic engine exit speeds.

To address these limitations we recommend the following prioritized extensions. First, perform transient LES or hybrid RANS–LES simulations at higher spatial and temporal resolution to capture vortex–plume interactions and their effect on peak and temporal persistence of supersaturation. Second, couple the CFD solver to a microphysics package capable of treating homogeneous/heterogeneous nucleation, droplet growth, and freezing kinetics (including the effect of soot and non-soot nuclei). Third, upgrade the thermophysical model to multi-species, non-ideal gas formulations (and include temperature-dependent transport properties) to better represent high- and low-temperature behaviour. Fourth, carry out a systematic sensitivity and uncertainty quantification study across flight altitudes, ambient temperatures, and

realistic engine exhaust speeds, and validate simulation trends with targeted laboratory or engine-test measurements where possible. Combined, these efforts will enable more definitive statements about whether hydrogen propulsion increases, decreases, or leaves unchanged the overall contrail mediated climate forcing of aviation.

References

[1] Gössling, S., and Humpe, A., "The global scale, distribution and growth of aviation: Implications for climate change," *Global Environmental Change*, Vol. 65, 2020, p. 102194. https://doi.org/https://doi.org/10.1016/j.gloenvcha.2020.102194, URL https://www.sciencedirect.com/science/article/pii/S0959378020307779.

[2] Teoh, R., Engberg, Z., Schumann, U., Voigt, C., Shapiro, M., Rohs, S., and Stettler, M. E. J., "Global aviation contrail climate effects from 2019 to 2021," *Atmospheric Chemistry and Physics*, Vol. 24, No. 10, 2024, pp. 6071–6093. https://doi.org/10.5194/acp-24-6071-2024, URL https://acp.copernicus.org/articles/24/6071/2024/.

[3] Soleymani, M., Mostafavi, V., Hebert, M., Kelouwani, S., and Boulon, L., "Hydrogen propulsion systems for aircraft, a review on recent advances and ongoing challenges," *International Journal of Hydrogen Energy*, Vol. 91, 2024, pp. 137–171. https://doi.org/https://doi.org/10.1016/j.ijhydene.2024.10.131, URL https://www.sciencedirect.com/science/article/pii/S0360319924043295.

[4] Bier, A., Unterstrasser, S., Zink, J., Hillenbrand, D., Jurkat-Witschas, T., and Lottermoser, A., "Contrail formation on ambient aerosol particles for aircraft with hydrogen combustion: a box model trajectory study," *Atmospheric Chemistry and Physics*, Vol. 24, No. 4, 2024, pp. 2319–2344. https://doi.org/10.5194/acp-24-2319-2024, URL https://acp.copernicus.org/articles/24/2319/2024/.

[5] Ferreira, T., and Gorlé, C., "Large-eddy simulation of contrail formation from hydrogen-fueled aircraft," *Center for Turbulence Research Annual Research Briefs 2024*, Stanford University, Stanford, California, 2024, pp. 1–14.

[6] Lottermoser, A., and Unterstrasser, S., "High-resolution modeling of early contrail evolution from hydrogen-powered aircraft," *Atmospheric Chemistry and Physics*, Vol. 25, No. 14, 2025, pp. 7903–7924. https://doi.org/10.5194/acp-25-7903-2025, URL https://acp.copernicus.org/articles/25/7903/2025/.

[7] Yan, B., Sun, C., Feng, Q., Chen, J., Gao, Y., and Tao, C., "The Study of Hydrogen Volume Fraction Effects on the Flame Temperature of Turbulence Diffusion Propane Jet Flames," *Fire*, Vol. 7, No. 1, 2024. https://doi.org/10.3390/fire7010010, URL https://www.mdpi.com/2571-6255/7/1/10.

[8] Alabaş, H. A., "CFD study of jet fuel with ammonia - Hydrogen mixtures in a jet engine: Emissions and combustion characteristics analysis," *International Journal of Hydrogen Energy*, Vol. 142, 2025, pp. 140–150. https://doi.org/https://doi.org/10.1016/j.ijhydene.2025.05.306, URL https://www.sciencedirect.com/science/article/pii/S0360319925026102.

[9] Khan, M. M., Bashir, S., Khan, M. W., and Ajenifujah, O., "Reducing emissions and fuel consumption in supersonic aviation with ammonia hybrid engines," *International Journal of Hydrogen Energy*, Vol. 162, 2025, p. 150540. https://doi.org/https://doi.org/10.1016/j.ijhydene.2025.150540, URL https://www.sciencedirect.com/science/article/pii/S0360319925035396.

[10] Megill, L., and Grewe, V., "Investigating the limiting aircraft-design-dependent and environmental factors of persistent contrail formation," *Atmospheric Chemistry and Physics*, Vol. 25, No. 7, 2025, pp. 4131–4149. https://doi.org/10.5194/acp-25-4131-2025, URL https://acp.copernicus.org/articles/25/4131/2025/.

[11] Khou, J.-C., Ghedhaïfi, W., Vancassel, X., and Garnier, F., "Spatial Simulation of Contrail Formation in Near-Field of Commercial Aircraft," *Journal of Aircraft*, Vol. 52, No. 6, 2015, pp. 1927–1938. https://doi.org/10.2514/1.C033101.

[12] Cantin, S., Chouak, M., Morency, F., and Garnier, F., "Effects of Fuel Sulfur Content and Non-Volatile PM Emissions on Contrail Formation: A CFD–Microphysics Study Including the Role of Organics," *Journal of Aerosol Science*, Vol. 188, 2025, p. 106612. https://doi.org/10.1016/j.jaerosci.2025.106612.

[13] Tegethoff, K., and Wheeler, A. P. S., "Non-Equilibrium Phase Changes in Aircraft Exhaust: A Computational Study on Early Contrail Formation," *arXiv preprint*, 2025.

[14] Lottermoser, A., and Unterstrasser, S., "Towards Intermediate Complexity Modelling of Contrail Formation: The New Dynamical Framework RadMod," *The Aeronautical Journal*, Vol. 129, 2025, pp. 351–379. https://doi.org/10.1017/aer.2024.130.

[15] Bier, A., Unterstrasser, S., Vancassel, X., and Gierens, K., "Engine Parameter Sensitivity of Contrail Formation in Hydrogen and Kerosene Combustion," *EGUsphere Discussions*, 2025. https://doi.org/10.5194/egusphere-2025-3708.

[16] OpenCFD Ltd., *rhoSimpleFoam — Steady-state solver for compressible turbulent flow of perfect gases*, OpenCFD Ltd., Dec. 2023. URL https://doc.openfoam.com/2312/tools/processing/solvers/rtm/compressible/rhoSimpleFoam/, openFOAM v2312 Documentation.

[17] Open Cascade SAS and CEA/DEN, EDF R&D, *SALOME Platform Documentation*, SALOME Project, 2025. URL https://www.salome-platform.org/?page_id=374.

[18] Kitware, Inc., "ParaView," , 2025. URL https://www.paraview.org/, version 5.12.1, open-source, multi-platform data analysis and visualization application.

[19] Atkins, P., and de Paula, J., *Physical Chemistry*, 5th ed., McGraw-Hill Education, New York, NY, 2009. ISBN-10: 0073048593.

[20] Tetens, O., "Über einige meteorologische Begriffe," *Zeitschrift für Geophysik*, Vol. 6, 1930, pp. 297–309. In German. Presents the empirical vapour-pressure formula commonly used in meteorology.